

X-Ray View of the Shock Front in the Merging Cluster Abell 3376 with Suzaku*

Hiroki AKAMATSU,¹ Motokazu TAKIZAWA,² Kazuhiro NAKAZAWA,³ Yasushi FUKAZAWA,⁴
 Yoshitaka ISHISAKI,¹ and Takaya OHASHI¹

¹ *Department of Physics, Tokyo Metropolitan University, 1-1 Minami-Osawa, Hachioji, Tokyo 192-0397*

² *Department of Physics, Yamagata University, Kojirakawa-machi 1-4-12, Yamagata 990-8560*

³ *Department of Physics, The University of Tokyo, 7-3-1 Hongo, Bunkyo-ku, Tokyo 113-0033*

⁴ *Department of Physical Science, Hiroshima University, 1-3-1 Kagamiyama, Higashi-hiroshima, Hiroshima 739-8526*
h_aka@phys.se.tmu.ac.jp

(Received (reception date); accepted (accepted date))

Abstract

We report on a Suzaku measurement of the shock feature associated with the western radio relic in the merging cluster A 3376. The temperature profile is characterized by an almost flat radial shape with $kT \sim 4$ keV within $0.5r_{200}$ and a rise by about 1 keV inside the radio relic. Across the relic region ($0.6 - 0.8r_{200}$), the temperature shows a remarkable drop from about 4.7 keV to 1.3 keV. This is a clear evidence that the radio relic really corresponds to a shock front possibly caused by a past major merger. The observed sharp changes of the temperature and electron density indicate the Mach number $\mathcal{M} \sim 3$. The radial entropy profile is flatter than the prediction ($r^{1.1}$) of numerical simulations within $0.5r_{200}$, and becomes steeper around the relic region. These observed features and time-scale estimation consistently imply that the ICM around the radio relic has experienced a merger shock and is in the middle of the process of dynamical and thermal relaxation.

Key words: galaxies: clusters: individual (Abell 3376) — galaxies: intergalactic medium — shock waves — X-rays: galaxies: clusters

1. Introduction

Clusters of galaxies are believed to grow through gas accretion from large-scale filaments and mergers of subclusters. Cluster mergers are the most energetic events in the Universe after the Big Bang with the total kinetic energy of the colliding subclusters reaching 10^{65} ergs. The kinetic energy is converted to thermal energy by driving shocks and turbulence. Existence of mega-parsec scale radio emission (halos and relics) in merging clusters indicates that those shocks and turbulence operate as main mechanisms of particle acceleration (see Ferrari et al. 2008 and reference therein). Radio relics are considered to be the synchrotron emission generated through the interaction between relativistic electrons, accelerated by a shock, and amplified magnetic field in the intracluster medium (ICM). Although these radio features provide direct evidence of particle acceleration, the detection of non-thermal (hard) X-ray emission caused by relativistic particles is still controversial (Nevalainen et al. 2004; Ajello et al. 2009). Currently, hard X-ray observations set lower limits of magnetic fields in ICM (Wik et al. 2009; Sugawara et al. 2009; Clarke & Ensslin 2006). Based on recent studies, it is believed that magnetic field of $0.1\text{--}10\text{ }\mu\text{G}$ exists in ICM.

Theoretical studies of cluster merger shocks provide rich information about the magnetic field, turbulence, particle acceleration and their time evolution (see e.g. Brüggen et al. 2011 for a review). Merger shocks are characterized by a Mach number $\mathcal{M} \lesssim 3$, causing amplification of magnetic fields to $B \sim 10\text{ }\mu\text{G}$ and production of relativistic particles (Takizawa

& Naito 2000; Takizawa 2008). Also, turbulence is considered to give a significant pressure support in the outer regions, with around 10% of the thermal pressure at least for a few Gyr after a major merger (Parrish et al. 2011). Recent numerical simulations include interaction of merger shocks with the filamentary cosmic web structures outside of clusters, and the results indicate that shock fronts are more enhanced in the filament direction (Paul et al. 2011).

Though past X-ray observations have shown images and temperature structures of cluster mergers, there are only few clusters for which clear evidence of the shocks has been obtained (1E0657-56, A520, and A2146: Markevitch et al. 2005; Clowe et al. 2006; Russell et al. 2010). The low X-ray surface brightness in the outer regions has hampered precise measurements of gas temperature and density in the pre-shock region in particular. Recently, existence of shock fronts with a Mach number of about 2 was confirmed in the radio relic region of A 3667 (Finoguenov et al. 2010; Akamatsu et al. 2011b). Additionally, a remarkable radio relic indicated a shock front with a Mach number of 4.6 based on the measurement of radio spectral index (CIZA2242: van Weeren et al. 2010). Thus, radio relics are the good probe to identify merger shocks and combination with X-ray data will yield important information about the gas dynamics associated with cluster mergers. Since the radio relics are mainly found in the outskirts of clusters where the gas density is low, sensitive X-ray observations are needed, especially in the upstream side of the shocks. The X-ray data will allow us to estimate the parameters of the gas and the magnetic field, and enable us to look into the actual process occurring during the cluster evolution.

In this paper, we present a new X-ray evidence of the

* Last update: 2018 November 19

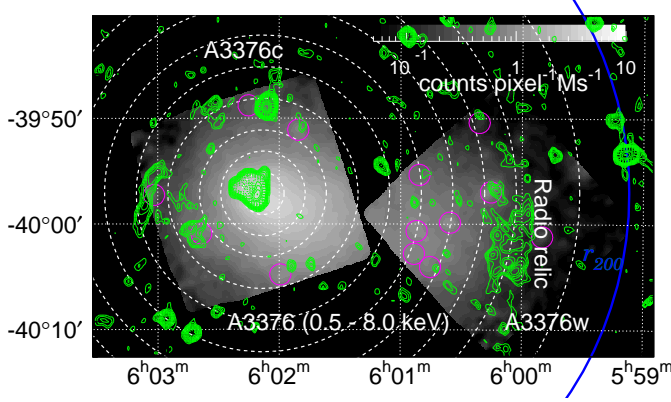


Fig. 1. X-ray image of A 3376 in the energy band 0.5–8.0 keV, after subtraction of the NXB with no vignetting correction and after smoothing by a 2-dimensional Gaussian with $\sigma = 16$ pixel $\approx 17''$. The large blue circle shows the virial radius of A 3376 with $r = 34'.6$, and white dotted circles show the annular regions used for the spectral analysis. Small magenta circles show point sources which are detected by *wavdetect* (see text). The VLA 1.4 GHz radio image is shown with green contours.

shock associated with the radio relic in Abell 3376, a well-known merging cluster with irregular morphology at $z = 0.046$. Previous studies showed the global mean temperature to be 4.0 keV and the existence of a pair of Mpc-scale radio relics revealed by 1.4 GHz VLA NVSS observations (Bagchi et al. 2006). Another feature of A 3376 is the report of the hard X-ray signal with BeppoSAX/PDS (Nevalainen et al. 2004). However, Suzaku HXD observation gave an upper limit which did not exclude the BeppoSAX flux (Kawano et al. 2009). We need to await further sensitive observations in the hard X-ray band.

We use $H_0 = 70 \text{ km s}^{-1} \text{ Mpc}^{-1}$, $\Omega_M = 0.27$ and $\Omega_\Lambda = 0.73$, respectively, which give 54 kpc per arcminute at $z = 0.046$. The virial radius is approximated by $r_{200} = 2.77 h_0^{-1} (\langle T \rangle / 10 \text{ keV})^{1/2} / E(z) \text{ Mpc}$, where $E(z) = (\Omega_M(1+z)^3 + 1 - \Omega_M)^{1/2}$ (Henry et al. 2009). For our cosmology and redshift, r_{200} is 1.86 Mpc ($= 34'.6$) with $kT = 4.7 \text{ keV}$. We employ solar abundance defined by Anders & Grevesse (1989) and Galactic absorption with $N_H = 5.8 \times 10^{20} \text{ cm}^{-2}$ (Dickey & Lockman 1990). Unless otherwise stated, the errors correspond to 90% confidence for a single parameter.

2. Observations and Data Reduction

As shown in Fig. 1, Suzaku carried out two pointing observations of Abell 3376 along the merger axis in October and November 2005, designated as A 3376c, A 3376w for the center and the west relic. The observation log is summarized in Table 1. All the observations were performed with either normal 5×5 or 3×3 clocking mode. The combined observed field extends to the virial radius of A 3376 ($34'.6 \sim 1.86 \text{ Mpc}$) indicated with blue circle in Fig. 1.

The XIS instrument consists of 4 CCD chips: one back-illuminated (BI: XIS1) and three front-illuminated (FI: XIS0, XIS2, XIS3) ones. Even A 3376 observations were carried out only 3–4 months after the launch, the IR/UV block-

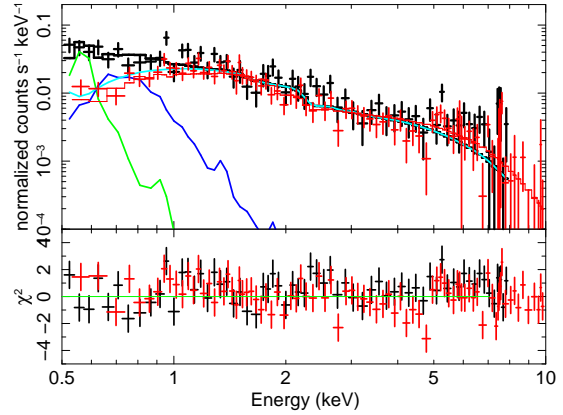


Fig. 2. The spectrum of the Q0551 field used for the background estimation, after subtraction of NXB and the source. The XIS BI (black) and FI (red) spectra are fitted with CXB + Galactic components (LHB, MWH) (*apecc+wabs(apecc+powerlaw)*). The CXB spectrum is shown with a black curve, and the LHB and MWH components are indicated by green and blue curves, respectively.

ing filters had some contamination accumulated at the time of the observations. We included its effect and uncertainty on the soft X-ray effective area in our analysis. We used HEASoft version 6.11 and CALDB 2011-06-30 for all the Suzaku data analysis presented here. We performed event screening with the cosmic-ray cut-off rigidity (COR) $> 8 \text{ GV}$ to increase the signal to noise ratio. We extracted pulse-height spectra in 10 annular regions whose boundary radii were $2', 4', 6', 9', 12', 15', 18', 21', 24', 27'$ and $31'$, with the center at ($06^{\text{h}}01^{\text{m}}00^{\text{s}}, -39^{\circ}57'07''$). We analyzed the spectra in the 0.5–10 keV range for the FI detectors and 0.5–8 keV for the BI detector. The energy range of 1.7–1.9 keV was ignored in the XIS spectral fitting, because the response matrix around Si-K edge had some residual uncertainties¹. In all annuli, positions of the calibration sources were masked out using the *calmask* calibration database (CALDB) file.

3. Spectral Fitting

3.1. Method of Spectral Fits

In the analysis of A 3376 data, we followed our previous analysis for the Suzaku observation of A 3667 (Akamatsu et al. 2011b), which shared many similar features but with much brighter surface brightness than the present object. The basic method of the spectral fit is described in subsection 4.1 of Akamatsu et al. (2011b). The observed spectrum was assumed to consist of thin thermal plasma emission from the ICM, the local hot bubble (LHB) and the milky way halo (MWH) as the Galactic foreground components, cosmic X-ray background (CXB) and non-X-ray background (NXB). The NXB component was estimated from the dark Earth database by the *xisnxbgen* FTOOLS (Tawa et al. 2008) and was subtracted from the data before the spectral fit. To adjust for the long-term variation of the XIS background due to radiation damage, we accumulated the NXB data for the period between 50 days before till 150 days after the observation of A 3376.

¹ <http://heasarc.nasa.gov/docs/suzaku/analysis/sical.html>

Table 1. Suzaku observations of A 3376 and the background region.

Target (Obs. ID)	Position (R.A., Decl.)	Start time (UT)	Exposure* (ks)	Exposure† (ks)
A 3376c (100034010)	(90.56, −39.94)	2005/10/06 14:46:08	110.4	78.0
A 3376w (800011010)	(90.05, −39.98)	2005/11/07 14:15:05	120.0	99.9
Q 0551-3637 (703036020)	(88.19, −36.63)	2008/05/14 13:25:55	18.8	15.3

*: no selection with COR2 †: COR2 > 8 GV

The spectrum of the Galactic background emission can be represented by two thin-thermal plasma models, by *appec* with 1 solar abundance. The estimation of the Galactic component and CXB is described in subsection 3.2. Because the Galactic and CXB components have almost uniform spatial distribution in the XIS field of view, we generate uniform auxiliary response files (ARF) for those emission. As for the ICM emission, we generated the ARF assuming the β -model surface brightness with $\beta = 0.40$, and $r_c = 2'.03$ (Cavagnolo et al. 2009) using *xissimarfgen* (Ishisaki et al. 2007).

For the spectral fits, we used XSPEC ver12.7.0. We carried out spectral fit to the pulse-height spectrum in each annular region separately. In the simultaneous fit of the BI and FI data, only the normalizations were allowed to be different between them, although we found that the derived normalizations were quite consistent between the two within 15%. In the central regions within $25'.2$, free parameters were temperature kT , normalization *norm* and metal abundance Z of the ICM component. In the outer regions ($> 25'.2$), we fixed the ICM metal abundance to 0.2 as reported by Kawano et al. (2009).

The 0.1–2.4 keV luminosity of A 3376 ($L_X = 2.5 \times 10^{44}$ erg s $^{-1}$) is less than 1/3 of the A 3667 value ($L_X = 8.8 \times 10^{44}$ erg s $^{-1}$), based on the ROSAT X-ray-brightest Abell-type clusters survey (Ebeling et al. 1996). To examine the effect of flux contamination from different spatial regions, we estimated mutual photon contributions among all the annuli (see Appendix. 1). The resultant photon fractions show that most of the detected photons come from the “on-source” region and about 20% is from the adjacent annular regions. These flux contamination features are very similar to that in A 3667 (Akamatsu et al. 2011b), in which the effect of stray light is always smaller than the systematic error of NXB.

Recent study of the stray light properties of Suzaku XRT (Takei et al. 2011) showed that its effect was significantly lower when the observing roll angle was inclined by 45 degrees just as in the case of the A 3376 west relic pointing. Based on this estimation, we can expect that the effect of the stray light does not influence the result significantly. We will not deal with the stray light any further in this paper.

3.2. Estimation of the Background Components

To exclude the point source contamination, we use *wavdetect* tool in CIAO package version 4.3.0² to identify point-like sources. We adopt the value of the *sigthresh* parameter as 5×10^{-6} in *wavdetect*, which is the significance threshold for the source detection. As shown by magenta circles in Fig. 1, we detected 12 point-like sources and masked out the regions

with 1 arcmin radius from the sources. The lowest detected 2–10 keV flux of these sources was $S_c = 5 \times 10^{-14}$ erg cm $^{-2}$ s $^{-1}$. Since this flux limit is lower than the level of $S_c = 2 \times 10^{-13}$ erg cm $^{-2}$ s $^{-1}$ by Kushino et al. (2002), we adopted the CXB intensity as 5.97×10^{-8} erg cm $^{-2}$ s $^{-1}$ sr $^{-1}$ after these point sources were subtracted. We also estimated the fluctuation of the CXB intensity based on Akamatsu et al. (2011a). Table 3 shows the resultant CXB fluctuation assuming the flux limit as $S_c = 5 \times 10^{-14}$ erg cm $^{-2}$ s $^{-1}$.

Since A 3376 is located far from the Galactic center ($l = 246.53^\circ$, $b = -26.29^\circ$), we did not consider contribution from the emission associated with the Galactic plane. To estimate the Galactic background, we use another Suzaku observation data for Q 0551-3637 (Observation ID: 703036020, Hereafter Q0551) at $3^\circ.8$ from A 3376 as shown in Table 1. We excluded the region of the main source Q0551 with a radius of $3'$. Using the data in the Q0551 field, we evaluated the model of the Galactic background described in Sec 3.1 with $N_H = 3.2 \times 10^{20}$ cm $^{-2}$. For the fitting, we fixed the temperature of the LHB component to 0.08 keV. The spectrum was well fitted with the above model ($\chi^2_\nu = 1.08$ for 135 degrees of freedom). The resultant parameters are shown in Table 2. The temperature of the MWH is $0.27^{+0.06}_{-0.03}$ keV, and the temperature and intensity are consistent with the typical Galactic emission. For the estimation of the systematic error of the background spectrum, we adopted the CXB fluctuation as 15%, and the OBF contamination to be $\pm 10\%$, respectively.

In the next section, we also examined the effect of systematic errors on our spectral parameters. We considered the systematic error for the NXB intensity to be $\pm 4.5\%$ (Tawa et al. 2008), the fluctuation of the CXB as shown in Table 3, and the OBF contamination to be $\pm 10\%$, respectively. The resultant parameters after taking into account the systematic errors are shown in Table 2.

3.3. Single-Temperature Fit

The pulse-height spectra and the best-fit models for all the annular regions are shown in Fig. 3. The parameters and the resultant χ^2 values are listed in Table 4. Considering both the statistical and systematic errors, the ICM signal was significantly detected out to $31'$ (1.67 Mpc $\sim 0.9r_{200}$) for the first time.

Fig. 4 shows radial profiles of ICM parameters (temperature, surface brightness, deprojected electron density, and thermal pressure). The temperature within $20'$ (1.2 Mpc corresponding to $0.6r_{200}$) of the cluster center shows an almost flat or rising profile with $kT \sim 4.0$ keV, which is very much different from those seen in the relaxed clusters. The increase of temperature

² <http://cxc.harvard.edu/ciao/>

Table 2. Best-fit background parameters

	NOMINAL	CXBMAX	CXBMIN	CONTAMI+10%	CONTAMI-10%
LHB					
$kT(\text{keV})$	0.08 (fix)	0.08 (fix)	0.08 (fix)	0.08 (fix)	0.08 (fix)
$norm^* (\times 10^{-3})$	$11.3^{+3.4}_{-3.8}$	$10.6^{+3.2}_{-3.7}$	$11.4^{+3.2}_{-3.4}$	$9.2^{+3.3}_{-4.5}$	$6.9^{+3.2}_{-3.4}$
MWH					
$kT(\text{keV})$	$0.27^{+0.06}_{-0.03}$	$0.28^{+0.06}_{-0.04}$	$0.28^{+0.06}_{-0.04}$	$0.27^{+0.06}_{-0.04}$	$0.27^{+0.06}_{-0.04}$
$norm^* (\times 10^{-4})$	$4.1^{+1.9}_{-1.5}$	$4.6^{+1.9}_{-1.4}$	$4.7^{+1.9}_{-1.4}$	$5.2^{+2.2}_{-1.4}$	$4.0^{+1.8}_{-1.4}$
$\chi^2/\text{d.o.f.}$	143 / 135	147 / 135	152 / 135	145 / 135	143 / 135

*: Normalization of the *apec* component scaled with a factor $1/400\pi$.

Norm = $\frac{1}{400\pi} \int n_e n_H dV / (4\pi(1+z^2)D_A^2) \times 10^{-14} \text{ cm}^{-5} \text{ arcmin}^{-2}$, where D_A is the angular diameter distance to the source.

Table 3. Estimation of the CXB fluctuation.

Region	0'-2'0	2'0-4'0	4'0-6'0	6'0-9'0	12'0-15'0	15'0-18'	18'-21'	21'-24'	24'-27'	27'-31'
SRR^*	4.01	3.35	3.29	3.40	0.36	0.76	1.08	0.95	0.83	0.66
$\Omega_{e,\text{Suzaku}}^\dagger$	12.4	18.0	30.3	50.2	12.6	34.6	60.7	64.5	67.0	63.7
$\sigma/I_{\text{CXB}}^\ddagger$	47.1	39.1	30.1	23.1	28.2	21.3	20.6	20.3	20.8	20.2

*: $SOURCE_RATIO_REG[\%]$ (See Akamatsu et al. 2011a Sec 3.4)

† : [arcmin²]

‡ : $S_c = 5 \times 10^{-14} \text{ erg cm}^{-2} \text{ s}^{-1}$ is assumed for all regions.

Table 5. The best fit parameters of 2 kT model with statistical and systematic errors (CXB fluctuations and OBF contamination)

2 kT	
kT_{high}	$4.05 \pm 1.62 \pm 1.37 \pm 0.11$
kT_{low}	$1.09 \pm 0.22 \pm 0.25 \pm 0.07$
Z	0.2 (fix)
$norm_{\text{high}}^*$	$1.56 \pm 0.6 \pm 0.7 \pm 0.3$
$norm_{\text{low}}^*$	$0.12 \pm 0.03 \pm 0.8 \pm 0.2$
$\chi^2/\text{d.o.f.}$	329/306

*: Same as Table 4.

† : 10-40 keV power-law flux in units of

$10^{-14} \text{ erg cm}^{-2} \text{ s}^{-1} \text{ arcmin}^{-2}$

just inside of the radio relic (18'-21', and 21'-24') compared with the level in the inner region is significant by about 4σ . The temperature of A 3376 suddenly drops at the radio relic region from 4.7 keV to 1.3 keV. These features strongly suggest that there is a shock heating taking place in the relic region. The surface brightness profile also shows more than an order of magnitude drop at the same region.

Based on the same Suzaku data, Kawano et al. (2009) showed the temperature in the radio relic region to be $kT \approx 3.8$ keV. The region roughly corresponds to a combination of 21' - 24' and 24' - 27' in our analysis, and our temperatures of 4.7 keV and 3.1 keV for the two regions indicate that our results are consistent with the previous study.

We also calculated the thermal pressure profile, with the pressure defined as $P = n_e kT$. The deprojected electron density n_e was derived from the *apec* normalization as in Akamatsu et al. (2011a). As seen in Fig. 4, the deprojected electron density and pressure profiles show a remarkable drop across the radio relic, which strongly suggests existence of the shock front.

3.4. Spectral Features in the Radio Relic Region

The radio relic region was mostly covered by the deep Suzaku observation (~ 100 ks). In the radio relic of A 3667, Akamatsu et al. (2011b) examined the possibility of multi-temperature plasma using $2kT$ model and several *DEM* (Differential Emission Measure: Kaastra et al. 1996) models. They confirmed that the emission measure distribution is characterized by two peaks around the radio relic region. The sharp drop of temperature in the radio relic of A 3376 suggests that a multi-temperature model is needed to describe the spectrum. The data will allow us to examine the relative contributions from different temperature components.

To examine the multi-temperature feature in the radio relic region (24'-27'), we included additional thermal component ($2kT$) to the single temperature model. We then obtained an almost acceptable fit with $\chi^2/\text{d.o.f.} = 329/306$ (Table 5) compared with the single temperature case of 345/308. The rather low statistics of the spectrum hampered us to distinguish between the $2kT$ and $1kT$ models. The hot component temperature was derived as $kT_{\text{high}} = 4.05 \pm 1.62$ keV, and the cool one as $kT_{\text{low}} = 1.09 \pm 0.22$ keV, while the common abundance was fixed to 0.2 solar. These values seem reasonable considering the result of the single temperature fit, which gave $kT = 3.11 \pm 1.10$ keV. These two temperature values are close to those observed inside and outside of the radio relic regions.

The actual three dimensional structure of the shock front would be a "bow" shape. Considering that the observed data should contain both the upstream and downstream components with respect to the shock front, it is natural to expect that the data in the radio relic region of A 3376 is a mixture of high and low temperature ICM by the projection effect. The ratio of emission measures can be used to constrain the shock front structure, however we leave such a study for future works.

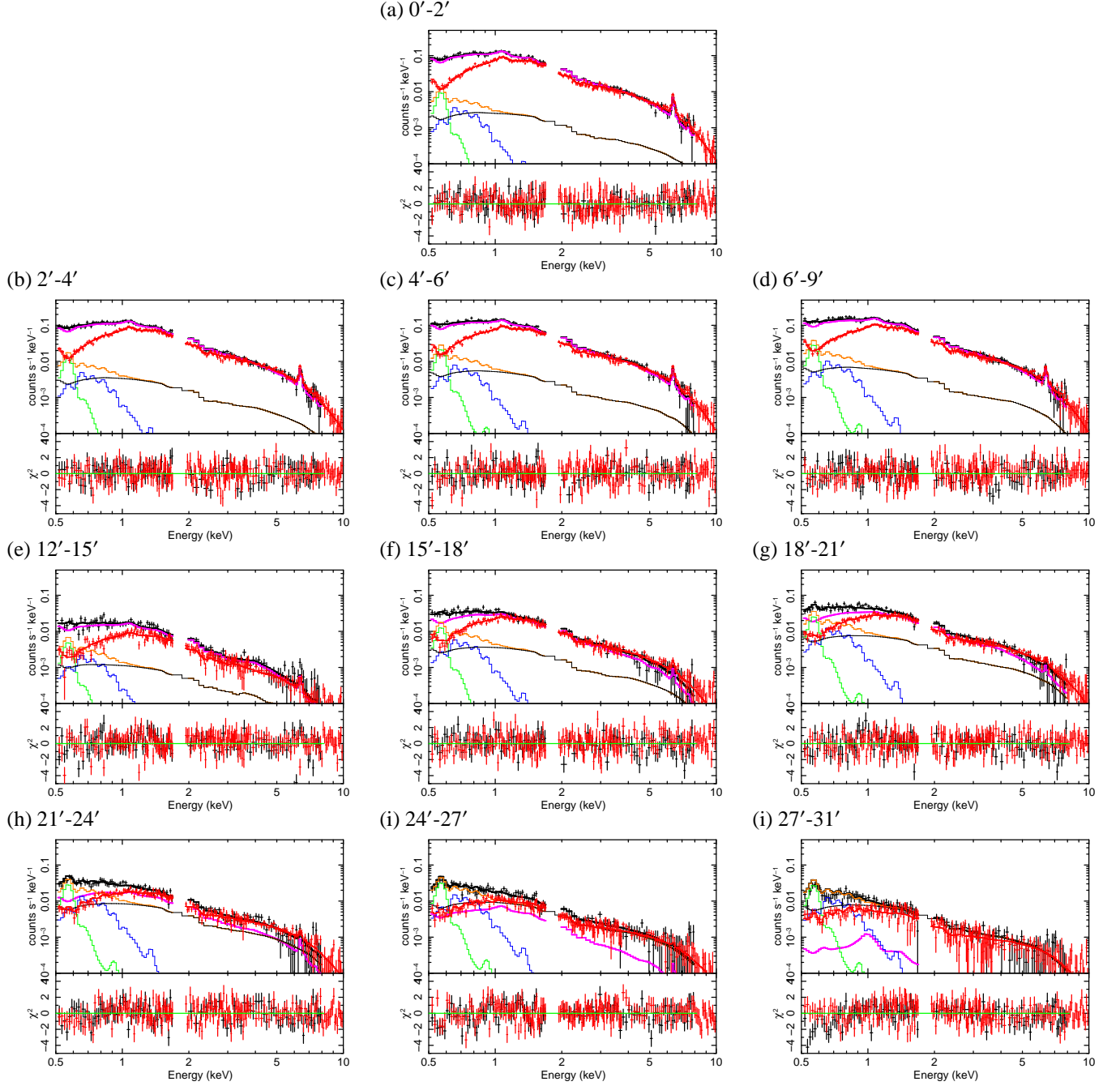


Fig. 3. NXB subtracted spectra in each annular region. The XIS BI (black) and FI (red) spectra are fitted with the ICM model ($wabs + apec$), along with the sum of the CXB and the Galactic emission ($apec + wabs(apec + powerlaw)$). The CXB component is shown with a black curve, and the LHB and MWH emissions are indicated by green and blue curves, respectively. The total background components are shown by the orange curve.

Table 4. Best-fit parameters of the ICM

	0'–2'	2'–4'	4'–6'	6'–9'	12'–15'	15'–18'	18'–21'	21'–24'	24'–27'	27'–31'
NOMINAL										
kT (keV)	$4.09^{+0.08}_{-0.08}$	$4.16^{+0.09}_{-0.09}$	$4.14^{+0.09}_{-0.09}$	$4.17^{+0.09}_{-0.09}$	$4.08^{+0.29}_{-0.27}$	$4.17^{+0.23}_{-0.19}$	$4.81^{+0.29}_{-0.28}$	$4.68^{+0.48}_{-0.48}$	$3.11^{+1.10}_{-0.78}$	$1.34^{+0.69}_{-0.39}$
Z	$0.33^{+0.03}_{-0.03}$	$0.28^{+0.03}_{-0.03}$	$0.26^{+0.03}_{-0.03}$	$0.25^{+0.03}_{-0.03}$	$0.21^{+0.09}_{-0.08}$	$0.18^{+0.06}_{-0.06}$	$0.11^{+0.06}_{-0.06}$	0.2 (fix)	0.2 (fix)	0.2 (fix)
norm*	$164.8^{+3.2}_{-3.2}$	$108.3^{+1.9}_{-1.9}$	$75.0^{+1.1}_{-1.1}$	$64.7^{+1.3}_{-1.3}$	$46.4^{+2.3}_{-2.3}$	$25.5^{+0.9}_{-0.9}$	$15.3^{+0.5}_{-0.5}$	$6.7^{+0.3}_{-0.3}$	$2.1^{+0.2}_{-0.2}$	$0.3^{+0.2}_{-0.2}$
$S^{\dagger}_{0.4-10 \text{ keV}}$	$70.11^{+1.45}_{-1.45}$	$46.28^{+0.13}_{-0.13}$	$31.88^{+0.14}_{-0.14}$	$26.25^{+1.41}_{-1.41}$	$19.04^{+0.48}_{-0.48}$	$10.92^{+0.28}_{-0.28}$	$6.14^{+0.22}_{-0.22}$	$2.72^{+0.15}_{-0.15}$	$0.77^{+0.04}_{-0.04}$	$0.13^{+0.01}_{-0.01}$
$\chi^2/\text{d.o.f}$	322 / 307	314 / 307	388 / 307	342 / 307	362 / 307	352 / 307	348 / 307	351 / 308	345 / 308	361 / 308
CXB MAX+NXB 4.5% RED										
kT (keV)	$4.15^{+0.08}_{-0.08}$	$4.23^{+0.09}_{-0.09}$	$4.22^{+0.09}_{-0.09}$	$4.26^{+0.11}_{-0.09}$	$4.39^{+0.35}_{-0.28}$	$4.56^{+0.25}_{-0.25}$	$5.34^{+0.36}_{-0.28}$	$5.57^{+0.59}_{-0.48}$	$5.35^{+1.45}_{-1.00}$	$2.27^{+1.65}_{-1.91}$
Z	$0.33^{+0.03}_{-0.03}$	$0.28^{+0.03}_{-0.03}$	$0.26^{+0.03}_{-0.03}$	$0.26^{+0.03}_{-0.03}$	$0.20^{+0.09}_{-0.08}$	$0.19^{+0.06}_{-0.06}$	$0.12^{+0.06}_{-0.06}$	0.2 (fix)	0.2 (fix)	0.2 (fix)
norm*	$164.8^{+3.2}_{-3.2}$	$108.3^{+1.9}_{-1.9}$	$76.1^{+1.1}_{-1.1}$	$65.4^{+1.3}_{-1.3}$	$49.3^{+2.3}_{-2.3}$	$26.2^{+0.9}_{-0.9}$	$15.8^{+0.5}_{-0.5}$	$7.3^{+0.3}_{-0.3}$	$2.6^{+0.2}_{-0.2}$	$0.5^{+0.2}_{-0.2}$
$S^{\dagger}_{0.4-10 \text{ keV}}$	$70.95^{+1.48}_{-1.48}$	$46.89^{+0.13}_{-0.13}$	$32.32^{+0.14}_{-0.14}$	$26.57^{+1.41}_{-1.41}$	$20.35^{+0.55}_{-0.55}$	$11.36^{+0.28}_{-0.28}$	$6.45^{+0.24}_{-0.24}$	$3.02^{+0.17}_{-0.17}$	$1.07^{+0.06}_{-0.06}$	$0.21^{+0.02}_{-0.02}$
$\chi^2/\text{d.o.f}$	327 / 307	317 / 307	391 / 307	347 / 307	362 / 307	353 / 307	350 / 307	356 / 308	352 / 308	373 / 308
CXB MIN+NXB 4.5% ADD										
kT (keV)	$4.04^{+0.08}_{-0.08}$	$4.09^{+0.09}_{-0.09}$	$4.06^{+0.09}_{-0.09}$	$4.09^{+0.09}_{-0.09}$	$3.82^{+0.29}_{-0.29}$	$3.99^{+0.21}_{-0.20}$	$4.52^{+0.31}_{-0.28}$	$4.00^{+0.43}_{-0.40}$	$1.55^{+0.26}_{-0.21}$	$0.87^{+0.57}_{-0.47}$
Z	$0.33^{+0.03}_{-0.03}$	$0.28^{+0.03}_{-0.03}$	$0.26^{+0.03}_{-0.03}$	$0.25^{+0.03}_{-0.03}$	$0.22^{+0.09}_{-0.09}$	$0.18^{+0.06}_{-0.06}$	$0.12^{+0.06}_{-0.06}$	0.2 (fix)	0.2 (fix)	0.2 (fix)
norm*	$161.6^{+3.2}_{-3.2}$	$106.4^{+1.9}_{-1.9}$	$72.8^{+1.1}_{-1.1}$	$63.4^{+1.3}_{-1.3}$	$42.7^{+2.3}_{-2.3}$	$24.2^{+0.9}_{-0.9}$	$14.0^{+0.5}_{-0.5}$	$5.7^{+0.3}_{-0.3}$	$1.1^{+0.2}_{-0.2}$	$0.1^{+0.2}_{-0.1}$
$S^{\dagger}_{0.4-10 \text{ keV}}$	$69.04^{+1.37}_{-1.37}$	$45.49^{+0.11}_{-0.11}$	$31.25^{+0.11}_{-0.11}$	$25.76^{+1.37}_{-1.37}$	$17.53^{+0.39}_{-0.39}$	$10.31^{+0.28}_{-0.28}$	$5.68^{+0.19}_{-0.19}$	$2.29^{+0.12}_{-0.12}$	$0.41^{+0.02}_{-0.02}$	$0.04^{+0.01}_{-0.01}$
$\chi^2/\text{d.o.f}$	316 / 307	314 / 307	391 / 307	339 / 307	367 / 307	350 / 307	357 / 307	367 / 308	351 / 308	414 / 308
CONTAMI 10% ADD										
kT (keV)	$4.05^{+0.08}_{-0.08}$	$4.12^{+0.09}_{-0.09}$	$4.12^{+0.09}_{-0.09}$	$4.16^{+0.09}_{-0.09}$	$3.96^{+0.27}_{-0.27}$	$4.20^{+0.25}_{-0.20}$	$4.88^{+0.29}_{-0.28}$	$4.73^{+0.48}_{-0.46}$	$3.16^{+1.19}_{-0.80}$	$1.37^{+1.14}_{-0.40}$
Z	$0.32^{+0.03}_{-0.03}$	$0.28^{+0.03}_{-0.03}$	$0.26^{+0.03}_{-0.03}$	$0.26^{+0.03}_{-0.03}$	$0.21^{+0.09}_{-0.08}$	$0.18^{+0.06}_{-0.06}$	$0.12^{+0.06}_{-0.06}$	0.2 (fix)	0.2 (fix)	0.2 (fix)
norm*	$164.8^{+3.2}_{-3.2}$	$108.3^{+1.9}_{-1.9}$	$75.0^{+1.1}_{-1.1}$	$64.1^{+1.3}_{-1.3}$	$45.9^{+2.3}_{-2.3}$	$25.1^{+0.9}_{-0.9}$	$14.9^{+0.5}_{-0.5}$	$6.6^{+0.3}_{-0.3}$	$1.9^{+0.2}_{-0.2}$	$0.2^{+0.1}_{-0.1}$
$S^{\dagger}_{0.4-10 \text{ keV}}$	$70.12^{+1.69}_{-1.69}$	$46.10^{+0.42}_{-0.42}$	$31.69^{+0.29}_{-0.29}$	$25.92^{+1.63}_{-1.63}$	$34.94^{+1.59}_{-1.59}$	$10.77^{+0.21}_{-0.21}$	$6.03^{+0.25}_{-0.25}$	$2.64^{+0.16}_{-0.16}$	$0.72^{+0.04}_{-0.04}$	$0.06^{+0.01}_{-0.01}$
$\chi^2/\text{d.o.f}$	323 / 307	316 / 307	388 / 307	338 / 307	364 / 307	348 / 307	354 / 307	363 / 308	360 / 308	402 / 308
CONTAMI 10% RED										
kT (keV)	$4.12^{+0.08}_{-0.08}$	$4.18^{+0.09}_{-0.09}$	$4.15^{+0.09}_{-0.09}$	$4.16^{+0.09}_{-0.09}$	$3.94^{+0.27}_{-0.27}$	$4.21^{+0.26}_{-0.20}$	$4.89^{+0.29}_{-0.28}$	$4.61^{+0.47}_{-0.43}$	$2.59^{+1.00}_{-0.58}$	$1.29^{+0.64}_{-0.31}$
Z	$0.33^{+0.03}_{-0.03}$	$0.28^{+0.03}_{-0.03}$	$0.26^{+0.03}_{-0.03}$	$0.25^{+0.03}_{-0.03}$	$0.21^{+0.09}_{-0.08}$	$0.17^{+0.06}_{-0.06}$	$0.11^{+0.06}_{-0.06}$	0.2 (fix)	0.2 (fix)	0.2 (fix)
norm*	$161.6^{+3.2}_{-3.2}$	$106.4^{+1.9}_{-1.9}$	$73.9^{+1.1}_{-1.1}$	$64.7^{+1.3}_{-1.3}$	$46.1^{+2.3}_{-2.3}$	$25.3^{+0.9}_{-0.9}$	$15.1^{+0.5}_{-0.5}$	$6.6^{+0.3}_{-0.3}$	$2.0^{+0.2}_{-0.2}$	$0.3^{+0.2}_{-0.2}$
$S^{\dagger}_{0.4-10 \text{ keV}}$	$69.34^{+1.75}_{-1.75}$	$45.65^{+0.48}_{-0.48}$	$31.53^{+0.34}_{-0.34}$	$25.92^{+1.66}_{-1.66}$	$35.00^{+1.59}_{-1.59}$	$10.76^{+0.19}_{-0.19}$	$6.03^{+0.26}_{-0.26}$	$2.66^{+0.16}_{-0.16}$	$0.73^{+0.04}_{-0.04}$	$0.11^{+0.01}_{-0.01}$
$\chi^2/\text{d.o.f}$	317 / 307	315 / 307	390 / 307	338 / 307	362 / 307	347 / 307	349 / 307	349 / 308	333 / 308	356 / 308

*: Normalization of the *apec* component scaled with a factor SOURCE-RATIO-REG/ Ω_e from Table 3,

Norm = $\frac{\text{SOURCE-RATIO-REG}}{\Omega_e} \int n_e n_H dV / (4\pi(1+z^2)D_A^2) \times 10^{-20} \text{ cm}^{-5} \text{ arcmin}^{-2}$, where D_A is the angular diameter distance to the source.

†: Photon flux in units of $10^{-6} \text{ photons cm}^{-2} \text{ s}^{-1} \text{ arcmin}^{-2}$. Energy band is 0.4 - 10.0 keV.

Surface brightness of the *apec* component scaled with a factor SOURCE-RATIO-REG and Ω_e from Table 3.

Table 6. The best fit parameters of 1*kT* +PL model with statistical error

	18'–21'		21'–24'		24'–27'	
	PL ($\Gamma = 2.0$)	PL ($\Gamma = 2.5$)	PL ($\Gamma = 2.0$)	PL ($\Gamma = 2.5$)	PL ($\Gamma = 2.0$)	PL ($\Gamma = 2.5$)
kT	$4.94^{+0.29}_{-0.28}$	$4.96^{+0.32}_{-0.29}$	$4.80^{+0.47}_{-0.46}$	$4.78^{+0.49}_{-0.43}$	$3.11^{+1.26}_{-0.67}$	$3.10^{+1.05}_{-0.64}$
Z	$0.12^{+0.06}_{-0.06}$	$0.117^{+0.06}_{-0.06}$	$0.26^{+0.13}_{-0.11}$	$0.27^{+0.12}_{-0.12}$	0.2 (fix)	0.2 (fix)
norm*	$14.5^{+0.5}_{-0.4}$	$14.6^{+0.6}_{-0.6}$	$6.2^{+0.5}_{-0.3}$	$6.3^{+0.5}_{-0.3}$	$1.9^{+0.2}_{-0.3}$	$1.9^{+0.3}_{-0.2}$
Γ	2.0 (fix)	2.5 (fix)	2.0 (fix)	2.5 (fix)	2.0 (fix)	2.5 (fix)
Flux UL [†]	1.02	1.06	0.99	1.03	0.99	1.08
$\chi^2/\text{d.o.f}$	351/306	351/306	356/306	355/306	347/307	348/307

*: Same as Table 4.

†: 10–40 keV flux of the power-law component, in $10^{-14} \text{ erg cm}^{-2} \text{ s}^{-1} \text{ arcmin}^{-2}$

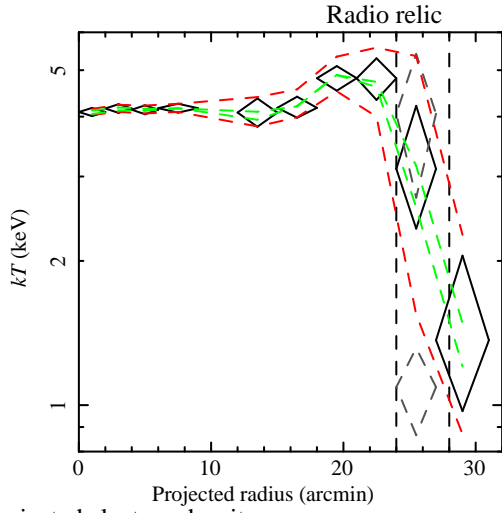
3.5. Constraint on Non-Thermal Emission

We evaluated the flux of the possible non-thermal X-ray emission using three XIS spectra around the radio relic region (Fig. 3g, h, i). Kawano et al. (2009) gave the 3σ upper limit flux for a power-law component in the radio relic region to be $1.1 \times 10^{-12} \text{ erg cm}^{-2} \text{ s}^{-1}$ in 4–8 keV and $1.9 \times 10^{-12} \text{ erg cm}^{-2} \text{ s}^{-1}$ with extrapolation to 15–50 keV, respectively, assuming the photon index to be 2.0. We added a power-law component to the above ICM model as: *apec*_{LHB} + *wabs* (*apec*_{MWH} + *powerlaw*_{CXB} + *apec*_{ICM} + *powerlaw*_{Non-thermal}). The depen-

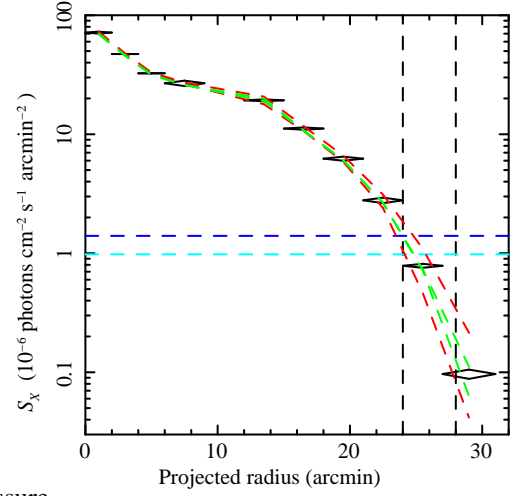
dence on the photon index was examined by adopting 2.0 and 2.5 in the fit.

The results of the spectral fits are summarized in Table 6. We found no significant difference against the photon index, and all three regions showed only upper limits for the power-law component. The derived upper-limit fluxes are $F_{10-40 \text{ keV}} < 1.1 \times 10^{-14} \text{ erg cm}^{-2} \text{ s}^{-1} \text{ arcmin}^{-2}$ at $\Gamma = 2.5$. To compare with the result by Kawano et al. (2009), we also derived the 4–8 keV flux as $F_{4-8 \text{ keV}} < 5.2 \times 10^{-15} \text{ erg cm}^{-2} \text{ s}^{-1} \text{ arcmin}^{-2}$. Using the solid angle covered by the radio relic ($\Omega_{\text{relic}} = 122 \text{ arcmin}^2$), the

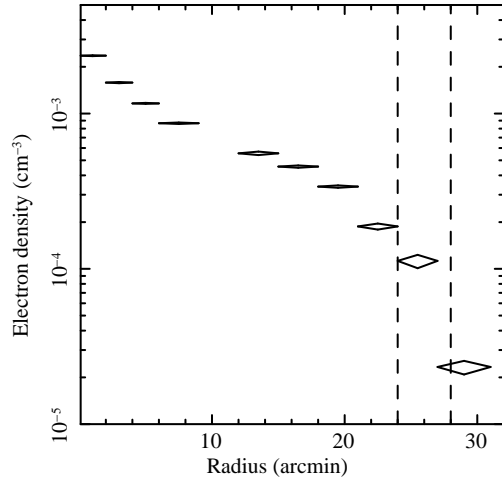
(a) Temperature



(b) Surface brightness



(c) Deprojected electron density



(d) Pressure

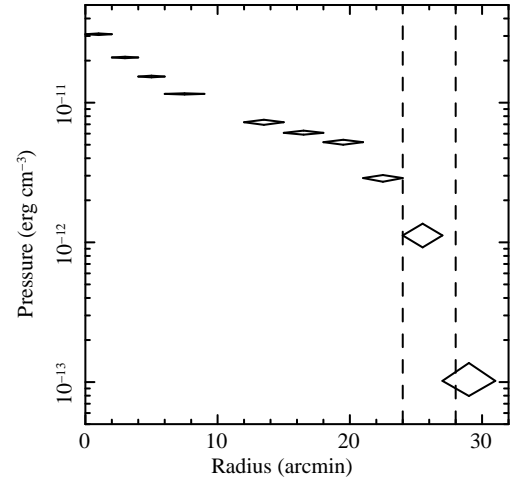


Fig. 4. Radial profiles of (a) ICM temperature, (b) surface brightness, (c) deprojected electron density, and (d) gas pressure. Suzaku best fit values with statistical errors are shown with black diamonds. Black dashed vertical lines show approximate radial boundaries of the west radio relic. Green and red dashed lines show typical systematic changes of the best-fit values due to change of OBF contaminants and NXB level. In temperature profile, gray dashed diamonds show the result of $2kT$ model fitting (see text). In surface brightness profile, blue and cyan dashed lines show the Galactic background and CXB emission, respectively.

flux upper limit in the 4–8 keV band is $5.3 \times 10^{-13} \text{ erg cm}^{-2} \text{ s}^{-1}$, which is consistent with the previous Suzaku results with XIS & HXD (Kawano et al. 2009). We note that the radial temperature profile shows an increase just inside of the radio relic over the level of the central region by about 1 keV. The result of the spectral fit implies that this increase is not due to the presence of a hard power-law emission but rather showing the pure ICM heating caused by the shock.

4. Discussion

Suzaku performed 2 pointing observations of Abell 3376 along its merger axis. The ICM temperature was found to be fairly flat at about 4 keV with a slow rise with radius in the region from the center to $0.6r_{200}$ (1 Mpc). This is followed by a sharp drop in the radio relic region, which implies there is a shock front. We will attempt to evaluate the gas properties

related with the shock (temperature, Mach number, magnetic field, and entropy) and discuss their implications.

4.1. Temperature Profiles

The ICM temperature is an important observational parameter which reflects the depth of the gravitational potential of the cluster. Their profiles also enable us to look into the history of the ICM heating and the growth of clusters.

Previous Chandra, XMM-Newton results for other clusters indicated a significant temperature decline toward the outer regions. Recent studies with Suzaku showed temperature profiles of ICM to the virial radius (r_{200}) for several clusters (George et al. 2008; Reiprich et al. 2009; Bautz et al. 2009; Hoshino et al. 2010; Kawaharada et al. 2010; Simionescu et al. 2011). These profiles for relaxed clusters are approximated by a “universal” profile which declines by a factor of ~ 3 at r_{200} from the center. On the other hand, merging clusters show complex temperature

distribution depending on the mass ratio and collision geometry. In the outer regions toward r_{200} , radial temperature profiles show some excesses and sharp drops which are not seen in relaxed systems (Akamatsu et al. 2011a; Akamatsu et al. 2011b). However, very little systematic studies have been made about the ICM properties in the outer regions of merging clusters.

We normalized the radial temperature profile by the average temperature determined within $0.4r_{200}$. Since A 3376 does not show a strong cool core, this should give a reasonable average temperature. The resulting scaled temperature profile is shown in Fig. 5 along with the previous Suzaku results (black crosses and diamonds: taken from Akamatsu et al. 2011a). Clearly, there is a marked difference between the profiles of relaxed and merging clusters. The relaxed clusters (black crosses) generally show a smooth decline from the center to the outer regions, consistent with the result of hydrodynamic simulations (Burns et al. 2010). Compared with these profiles, the A 3376 profile shows a large excess within $0.7r_{200}$ before the sharp drop at $0.7 - 0.8r_{200}$.

Numerical simulation of merging clusters by Paul et al. (2011) shows a shock feature very similar to the one in A 3376. This simulation after about 3 Gyr after a major merger shows an arc-like high temperature region whose width is about 200 kpc, very similar to the observed temperature enhancement in Fig. 5. This suggests that A 3376 is still evolving after several Gyrs elapsed from the last major merger.

The Λ CDM model predicts that clusters grow through sub-cluster mergers and matter accretion from large-scale structures. Those dynamical events should give strong impacts on the ICM temperature structure, such as seen in A 3376. Since the ICM density is very low in the cluster outskirts ($n_e = 10^{-5} - 10^{-3} \text{ cm}^{-3}$), the radiative cooling and conduction times are expected to be very long with the cooling time largely exceeding the age of the Universe. We can naturally expect that the temperature structure carries important information about the history of the cluster growth. However, as mentioned above, there are no clear signs of dynamical evolution in relaxed clusters. This indicates that the observed peculiar temperature structure in the merging clusters will be settled to the universal profile in a fairly short time scale, much shorter than the Hubble time. Since cooling time is too long, we have to consider other possibilities such as (i) ICM cooling by adiabatic expansion, and (ii) ICM diffusion caused by pressure gradient. We will discuss these time scales in section 4.4.

A fraction of the merger energy would be channeled into the acceleration of ultra-relativistic particles and amplification of magnetic fields. However, it is unknown that how these processes actually take place and distribute the merger energy to other forms in an efficient way. The turbulent motion can be detected through line broadening by X-ray microcalorimeters such as with SXS instrument on ASTRO-H (Mitsuda et al. 2010) and Athena, since X-ray calorimeters provide superior energy resolution by a factor of 20–30 better than that with the CCD instruments. The wealth of information will open a new window in our understanding of heating and particle acceleration caused by cluster merger shocks.

4.2. Mach Number

Recent studies with XMM-Newton and Suzaku showed sharp temperature drops at the region of the radio relic in A 3667 (Finoguenov et al. 2010; Akamatsu et al. 2011b). Finoguenov et al. (2010) reported a sharp edge in the surface brightness at the outer boundary of the NW radio relic in A 3667. Akamatsu et al. (2011b) reported a significant jump in the ICM parameters (temperature, surface brightness, electron density, and pressure) across the same relic. The derived Mach number is $\mathcal{M} \sim 2$.

We estimate the Mach number based on the Suzaku data in the same way as Akamatsu et al. (2011b). The Mach number can be obtained by applying the Rankine-Hugoniot jump condition,

$$\frac{T_2}{T_1} = \frac{5\mathcal{M}^4 + 14\mathcal{M}^2 - 3}{16\mathcal{M}^2}, \quad \frac{1}{C} = \frac{3}{4\mathcal{M}^2} + \frac{1}{4}, \quad (1)$$

where $C = \frac{n_{e2}}{n_{e1}}$ is the shock compression and subscripts 1 and 2 denote pre-shock and post-shock values, respectively, assuming the ratio of specific heats as $\gamma = 5/3$. Here, we assume the regions 21'–24' and 27'–31' to be the post and pre shock regions, respectively. Because the compression factor, C , exceeds the value for the strong shock limit, we only derived mach number from temperature jump. Table 7 shows the resultant Mach number, whose values are $\mathcal{M} = 2.94 \pm 0.77$ based on the jumps of temperature. Compared with other clusters which also show shock fronts (A520, 1E0657-558, A2246, A 3667: Markevitch et al. 2005; Clowe et al. 2006; Russell et al. 2010; Akamatsu et al. 2011b), the Mach number in A 3376 is slightly larger than the other cases.

We derive the compression factor, $C = 7.8 \pm 4.7$, which almost exceeds the value for the strong shock limit, even though with a large error. The electron density estimated here is based on the assumption of spherical symmetry, which is not strictly correct when the shock propagates along the merger axis. Since the spherical assumption relates the observed flux to a shell-like volume with a larger line-of-sight depth than the case of a relic volume, the density in particular for the pre-shock region is underestimated by a factor of roughly 1.5. In addition to this uncertainty, we checked the dependence on the centroid position of the spherical shock. We set the center of the sphere at the secondary X-ray peak which is closer to the radio relic. The resultant compression parameter is $C = 5.01$. This indicates that the determination of the centroid have a significant impact on the shock parameter, which is mainly resulted from the estimated line of sight depth of the shocked region.

The shock front in A 3376 is located far from the cluster center ($1.2 \text{ Mpc} \sim 0.6 r_{200}$) just as in A 3667. The temperature in the upstream region of the shock is $\sim 1 \text{ keV}$, indicating the pre-shock sound speed to be $v_{ss} \sim 520 \text{ km s}^{-1}$. Combining this with the shock compression C , we can evaluate the shock speed by $v_{\text{shock}} = C \cdot v_{ss}$ to be $> 2080 \text{ km s}^{-1}$ assuming $C = 4.0$ from the above discussion. The estimated shock speed well agrees with those in other clusters (1E0657-558: 4500 km s^{-1} , A520: 2300 km s^{-1}), but twice higher than the A 3667 case ($1360 \pm 120 \text{ km s}^{-1}$). The shock speed is large enough to account for the radio relic by a merger shock model (Takizawa & Naito 2000; Ricker & Sarazin 2001; Mathis et al. 2005). On

Table 7. Mach number estimation for A 3376 assuming $\gamma = 5/3$.

Parameter	Pre shock	Post shock	Mach number
kT [keV]	1.34 ± 0.69	4.68 ± 0.48	2.97 ± 0.77

the other hand, this v_{shock} seems too high considering the ICM temperature of 4 keV. We may need to consider a possibility that the true gas temperature is much higher than the measured electron temperature.

4.3. Entropy Profile

Theoretical studies of the ICM (Tozzi & Norman 2001; Voit et al. 2003) predicts the entropy profile approximated by $r^{1.1}$, assuming that the gravitational energy of the accreting gas is efficiently converted into the thermal energy. However, Chandra observations revealed that the entropy in the central regions of relaxed clusters often showed a flat profile (Cavagnolo et al. 2009). The origin of this behavior is considered to be the feedback of star formation and central AGN activities, which generate extra entropy (Peterson & Fabian 2006). Entropy profile is thus sensitive to the non-gravitational energy injection and can be used to explore such a process even in the outer regions of clusters.

We will define the “entropy” of the ICM by $K = kT \cdot n_e^{-2/3}$. Fig. 5 shows the resultant entropy profile of A 3376. The slope shows a large deviation from the standard value of 1.1 and close to 0.4 in the radius range 0.5–20.0. The solid black line shows $K \propto r^{0.4}$, compared with the solid gray line indicating $K \propto r^{1.1}$. Recent XMM-Newton study reported entropy profiles of 31 clusters (Pratt et al. 2010), and the distribution of the slope indicated a peak value of 0.98. Therefore, the slope of 0.4 is very unusual and can be regarded as a transient value occurring in a certain phase of cluster mergers.

The slope shows a steepening and flattening across the radio relic, which itself indicates the shock heating. A similar feature was also reported in A 3667 (Akamatsu et al. 2011b). The slope of A 3667 showed a marginal increase and a sudden drop across the radio relic region. In A 3376, the increase of the entropy slope is more significant, which suggests a stronger shock than in A 3667. This probably corresponds to the feature that the estimated Mach number in A 3376 is factor of 2 higher than in A 3667.

4.4. Relaxation Time Scales

As shown in the previous sections, A 3376 exhibits distinct ICM properties which are significantly different from those seen in the relaxed clusters. The density and temperature structures around the shock region, along with the irregular morphology of this cluster, suggest that A 3376 is a young system regarding the relaxation of the ICM. The fact that most of the relaxed clusters now attain almost universal temperature profile indicates that the time needed for the ICM to reach thermal and dynamical equilibrium is much shorter than the cluster life. In this section we evaluate several relevant time scales based on the present observational quantities.

We first estimate the time in which the shock front reaches the current position. Assuming that the shock has traveled the distance between the cluster center and the relic position with a

constant velocity ($v = 2000 \text{ km s}^{-1}$), the time required to propagate this length of $\sim 1.5 \text{ Mpc}$ is 0.32 Gyr.

Next, we estimate the time scale to attain thermal equilibrium after the shock heating. The shock heating should first act on ions rather than electrons, and then the thermal energy is transferred from ions to electrons through Coulomb collisions. The equilibration time scale between ion and electron is 3 orders of magnitude longer than the electron-electron timescale. Therefore, the cluster thermal time scale after the shock heating is limited by the electron-ion time scale. According to Takizawa (1998), the electron-ion equilibration timescale is given by

$$t_{\text{ie}} = 2 \times 10^8 \text{ yr} \left(\frac{n_e}{10^{-3} \text{ cm}^{-3}} \right)^{-1} \left(\frac{T_e}{10^8 \text{ K}} \right)^{3/2} \left(\frac{\ln \Lambda}{40} \right), \quad (2)$$

where $\ln \Lambda$ denotes the Coulomb logarithm (Spitzer 1956).

In the central region, this gives 0.03 Gyr, which is about 10 times shorter than the elapsed time after the shock passage. We calculated the elapsed time after the shock passage and the time for electron-ion equilibration t_{ie} as a function of radius. The resultant time scales are shown in Fig. 5 (c). Here, red diamonds show t_{ie} , and gray dashed diamonds are the ionization time scale t_i of Fe-K α assuming $n_e t = 3 \times 10^{12} \text{ cm}^{-3} \text{ s}$. Solid line shows the elapsed time after the shock passage, assuming the shock propagation from inner to outer regions. We can see that the elapsed time is shorter than t_{ie} outside of $0.6r_{\text{shock}}$ corresponding to $17'$ (920 kpc). This suggests that the electron temperature is likely to be lower than the ion temperature in the outer region including the radio relic (Akahori & Yoshikawa 2008; Akahori & Yoshikawa 2011). Those sign already reported another merging cluster RX J1347.5-1145 (Ota et al. 2008). In the region that t_i exceed the sound crossing time t_{sc} ($t_i > t_{\text{sc}}$), there will be non-equilibrium ionization state. The future high resolution X-ray spectroscopy can reveal those dynamical ionization states.

Finally, we estimate the time scale in which the sharp change of the temperature disappears. Those high temperature region will diffuse out due to the high pressure in the post-shock region and reach equilibrium in the sound crossing time ($t_{\text{sc}} = R/v_s$), where R is the width of the high temperature region and v_s is the sound speed, respectively. Using the observed temperature ($kT = 4.7 \text{ keV}$ which corresponds to $v_s = 1100 \text{ km s}^{-1}$) and the width of the high temperature region ($R = 320 \text{ kpc}$), we can calculate the sound crossing time. The resultant time scale is $t_{\text{sc}} = 0.28 \text{ Gyr}$.

In summary of this section, the observed features of temperature change, entropy slope and the time scale consideration all point to that the outer region ($> 1 \text{ Mpc}$) of A 3376 is not reaching the equilibrium. In this sense, A 3376 is still a very young system in view of the cluster evolution.

5. Summary

We observed Abell 3376 with Suzaku XIS and derived radial profiles of temperature, surface brightness, electron density, and thermal pressure. The temperature and surface brightness shows remarkable jumps across the radio relic, located at $\sim 1.5 \text{ Mpc}$ from the cluster center. We evaluated the Mach number using the Rankine-Hugoniot jump condition as $\mathcal{M} = 3.0$. The

(a) Normalized temperature profiles

(b) Entropy profiles

(c) Equilibrium time scale

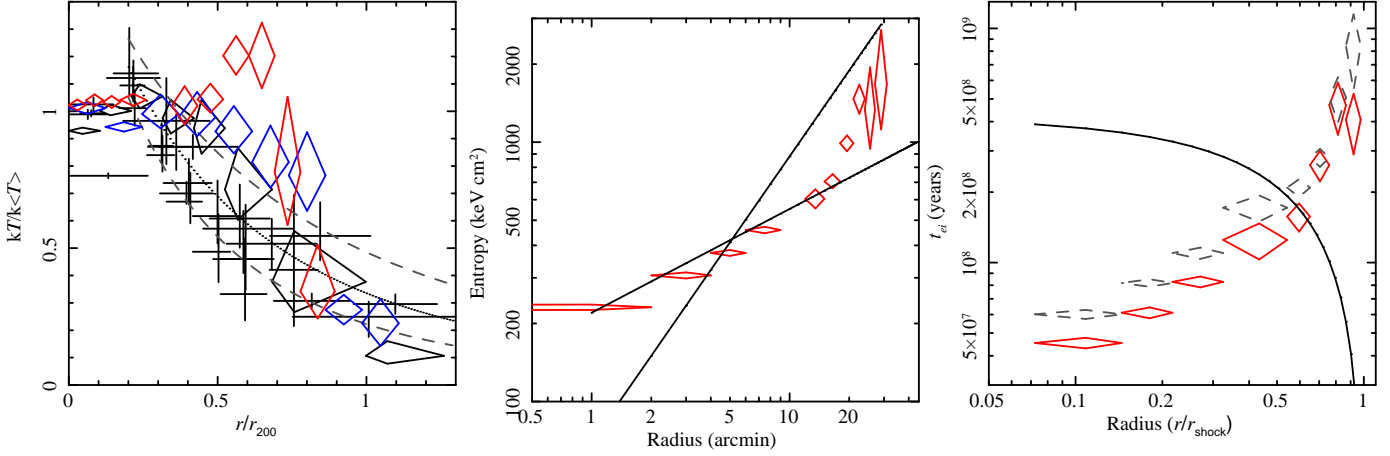


Fig. 5. Radial profiles of normalized temperature, entropy and equilibration time scale. (a) Scaled projected temperature profiles compared with relaxed clusters (Akamatsu et al. 2011a). The profiles have been normalized to the mean (within $0.4 r_{200}$) temperature. The r_{200} value is derived from Henry et al. (2009). Dotted line shows simulation result (Burns et al. 2010). Two gray dashed lines show standard deviation. Black crosses are for the relaxed clusters. Diamonds show merger clusters (black: A2142, blue: A3667, red: A3376). In entropy profile (b), black solid line shows $K \propto r^{1.1}$ given by Voit et al. 2003. (c) Ion-electron equilibration time scale. Horizontal scale is normalized by the radius of the radio relic. Solid curve shows the time after a shock heating assuming a constant shock speed $v = 2000 \text{ km s}^{-1}$. Red diamonds show the electron-ion equilibration time t_{ie} . Gray dashed diamond show the ionization time for $n_e t = 3 \times 10^{12} \text{ cm}^{-3} \text{ s}$.

main results on A 3376 are summarized as follows;

- The ICM temperature is fairly flat at about 4 keV in the radius range from the center to $0.6r_{200} \sim 1.1 \text{ Mpc}$, followed by a small enhancement near the radio relic to 5 keV.
- Across the radio relic region, the ICM parameters (temperature, electron density, and pressure) show significant jumps. The temperature drops from 4.5 keV to 1.0 keV, and the density and pressure both show an order of magnitude drop.
- The estimated Mach number of the shock is $\mathcal{M} = 2.97 \pm 0.77$ based on the temperature jump, leading to the shock speed of $v_{\text{shock}} > 2000 \text{ km s}^{-1}$.
- The temperature structure observed in A 3376 is markedly different from those in relaxed clusters, suggesting that this cluster is a young system with the ICM properties strongly influenced by the merger shock.
- The entropy profile is significantly flatter than the standard prediction of $r^{1.1}$ and is approximated by $r^{0.4}$, accompanied by slope changes across the radio relic. This indicates that the heating process is still going on in this region.
- Based on the measurement temperature and electron density, the ion-electron relaxation time is longer than the elapsed time after the shock passage near the shock region.

These results show that A 3376 is a dramatic merging cluster, with their outskirts still under a non-equilibrium condition. Because of the existence of the large scale shock front, future X-ray and SZ observations will provide new insight on the dynamical evolution of clusters.

The authors thank all the Suzaku team members for their support of the Suzaku project. We also thank an anonymous

referee for constructive comments. H. A. is supported by a Grant-in-Aid for Japan Society for the Promotion of Science (JSPS) Fellows (22-1582).

Appendix 1. Stray Light

To assess the effect of stray light from cluster core to outskirts, we calculated photon contribution from each region to “On-Source” region using *xissim* (Ishisaki et al. 2007). We use β -model ($\beta = 0.40, r_c = 2'.03$) surface brightness profiles for input image and observed spectral information for input spectrum. Table 8 shows the resultant photon fraction detected in each region. The “On-Source” fraction shows the highest value followed by those in the adjacent regions, which is naturally understood considering the point-spread function of the Suzaku XRT (Serlemitsos et al. 2007).

Appendix 2. ICM emission in the outermost region

Since the validity of our detection of the ICM emission in the outermost region, $r = 27' - 31'$, is important in this paper, we performed two additional checks. One is to look into the Suzaku spectrum by employing different background data, and the other is the analysis of the ROSAT pointing data for this cluster.

To examine the adequacy of our background estimation process, we incorporated another background data which were taken at 4 degrees offset from A3376 on TX COL (ObsID: 404031010). We evaluated the background components (MWH and LHB) in the same fashion as described in Sec 3.2. The resultant best-fit spectral parameters are shown in Table. 9. Compared with the previous background estimation (Table 2), the temperatures and normalizations are consistent within the statistical errors, indicating that our back-

Table 8. Relative count contributions (%) due to PSF broadening of the Suzaku XIS mirror. Most counts come from the “On-Source” region.

Detector/ Sky	(1)	(2)	(3)	(4)	(5)	(6)	(7)	(8)	(9)	(10)
(1) 0'0-2'0	71.4	26.2	1.9	0.4	0.1	0.0	0.0	0.0	0.0	0.0
(2) 2'0-4'0	22.3	62.6	13.5	1.3	0.2	0.0	0.0	0.0	0.0	0.0
(3) 4'0-6'0	3.7	25.1	58.3	12.2	0.6	0.0	0.0	0.0	0.0	0.0
(4) 6'0-9'0	1.2	3.2	18.7	70.2	6.4	0.1	0.1	0.1	0.0	0.0
(5) 12'0-15'0	0.2	0.3	0.9	10.6	76.3	10.1	1.0	0.3	0.0	0.2
(6) 15'0-18'0	0.1	0.2	0.0	0.3	11.7	70.3	15.9	1.1	0.2	0.1
(7) 18'0-21'0	0.0	0.2	0.2	0.2	1.8	13.4	68.4	14.7	0.9	0.2
(8) 21'0-24'0	0.2	0.2	0.2	0.1	0.7	1.3	17.0	65.9	13.7	0.6
(9) 24'0-27'0	0.2	0.4	0.3	0.4	0.5	0.7	1.6	20.0	66.3	9.7
(10) 27'0-31'0	0.2	0.3	0.2	0.4	0.7	0.3	1.0	2.5	21.3	73.1

ground estimation is appropriate. Using the above background components, we analyze the outermost region (27' – 31' annulus). The resultant best-fit values are $kT = 1.37^{+0.51}_{-0.33}$ keV and $\text{norm} = 0.3 \pm 0.2$, which are consistent with the original one.

Next, we derived the surface brightness of A3376 west direction using the ROSAT archival data (seqID: RP800154N00). We set the cluster center at ($20^{\text{h}}12^{\text{m}}31^{\text{s}}, -56^{\circ}49'12''$) and extracted a region with a width of 6' to the west from the A3376 center. We confirmed that the surface brightness dropped by an order of magnitude from $r = 20'$ to $30'$ (Fig.6). The brightness boundaries defined by the systematic error, mostly due to the background fluctuation, are indicated with blue histograms. Note that the ICM shows significant X-ray emission around $r = 30'$ even considering the systematic error (rp800154n00_bk1.fits). These results indicate the validity of the Suzaku detection of the ICM emission in the outermost region.

References

- Akahori, T., & Yoshikawa, K. 2011, arXiv:1109.0826
 Akahori, T., & Yoshikawa, K. 2008, PASJ, 60, L19
 Akamatsu, H., Hoshino, A., Ishisaki, Y., Ohashi, T., Sato, K., Takei, Y., & Ota, N. 2011, arXiv:1106.5653
 Akamatsu, H., et al. 2011, arXiv:1111.5162
 Ajello, M., Rebusco, P., Cappelluti, N., et al. 2009, ApJ, 690, 367
 Anders, E., & Grevesse, N. 1989, Geochim. Cosmochim. Acta, 53, 197
 Asai, N., Fukuda, N., & Matsumoto, R. 2004, Journal of Korean Astronomical Society, 37, 575
 Bagchi, J., Durret, F., Neto, G. B. L., & Paul, S. 2006, Science, 314, 791
 Bautz, M. W., et al. 2009, PASJ, 61, 1117
 Burns, J. O., Skillman, S. W., & O'Shea, B. W. 2010, ApJ, 721, 1105
 Brüggén, M., Bykov, A., Ryu, D., Röttgering, H. 2011, Space Sci. Rev., 138
 Cavagnolo, K. W., Donahue, M., Voit, G. M., & Sun, M. 2009, ApJS, 182, 12
 Clarke, T. E., & Ensslin, T. A. 2006, AJ, 131, 2900
 Clowe, D., Bradač, M., Gonzalez, A. H., Markevitch, M., Randall, S. W., Jones, C., & Zaritsky, D. 2006, ApJL, 648, L109
 Dickey, J. M., & Lockman, F. J. 1990, ARA&A, 28, 215
 Ebeling, H., Voges, W., Bohringer, H., et al. 1996, MNRAS, 281, 799
 George, M. R., Fabian, A. C., Sanders, J. S., Young, A. J., and Russell, H. R., 2008, MNRAS, 395, 657
 Ishisaki, Y., et al. 2007, PASJ, 59, 113
 Henry, J. P., Evrard, A. E., Hoekstra, H., Babul, A., & Mahdavi, A. 2009, ApJ, 691, 1307
 Hoshino, A., et al. 2010, PASJ, 62, 371
 Ferrari, C., Govoni, F., Schindler, S., Bykov, A. M., & Rephaeli, Y. 2008, Space Sci. Rev., 134, 93
 Finoguenov, A., Sarazin, C. L., Nakazawa, K., Wik, D. R., & Clarke, T. E. 2010, apj, 715, 1143
 Kaastra, J. S., Mewe, R., & Nieuwenhuijzen, H. 1996, UV and X-ray Spectroscopy of Astrophysical and Laboratory Plasmas, 411
 Kawaharada, M., et al. 2010, ApJ, 714, 423
 Kawano, N., et al. 2009, PASJ, 61, 377
 Kushino, A., Ishisaki, Y., Morita, U., Yamasaki, N. Y., Ishida, M., Ohashi, T., & Ueda, Y. 2002, PASJ, 54, 327
 Markevitch, M., Govoni, F., Brunetti, G., & Jerius, D. 2005, ApJ, 627, 733
 Mathis, H., Lavaux, G., Diego, J. M., & Silk, J. 2005, MNRAS, 357, 801
 Mitsuda, K., et al. 2010, Proc. SPIE, 7732,
 Nevalainen, J., Oosterbroek, T., Bonamente, M., & Colafrancesco, S. 2004, ApJ, 608, 166
 Ota, N., Murase, K., Kitayama, T., et al. 2008, A&A, 491, 363
 Parrish, I. J., McCourt, M., Quataert, E., & Sharma, P. 2011, arXiv:1109.1285
 Paul, S., Iapichino, L., Miniati, F., Bagchi, J., & Mannheim, K. 2011, ApJ, 726, 17
 Pratt, G. W., et al. 2010, A&A, 511, A85
 Peterson, J. R., & Fabian, A. C. 2006, Phys. Rep., 427, 1
 Reiprich, T. H., et al. 2009, A&A, 501, 899
 Ricker, P. M., & Sarazin, C. L. 2001, ApJ, 561, 621
 Russell, H. R., Sanders, J. S., Fabian, A. C., Baum, S. A., Donahue, M., Edge, A. C., McNamara, B. R., & O'Dea, C. P. 2010, MNRAS, 406, 1721
 Takei, Y., Akamatsu, H. et al. 2011, Suzaku Conference
 Tawa, N., et al. 2008, PASJ, 60, 11
 Serlemitsos, P. J., et al. 2007, PASJ, 59, 9
 Simionescu, A., et al. 2011, Science, 331, 1576
 Sugawara, C., Takizawa, M., & Nakazawa, K. 2009, PASJ, 61, 1293
 Spitzer, L. Jr., 1956, Physics of Fully Ionized Gases, New York: Interscience
 Takizawa, M., 1998, ApJ, 509, 579
 Takizawa, M. 2008, ApJ, 687, 951
 Takizawa, M., & Naito, T. 2000, ApJ, 535, 586
 Tozzi, P., & Norman, C. 2001, ApJ, 546, 63
 van Weeren, R. J., Röttgering, H. J. A., Brüggén, M., & Hoeft, M. 2010, Science, 330, 347

Table 9. Best-fit background parameters using TX COL

	$kT(\text{keV})$	$norm^* (\times 10^{-3})$	$kT(\text{keV})$	$norm^* (\times 10^{-3})$	$\chi^2/\text{d.o.f}$
NOMINAL	0.08 (fix)	$9.3^{+3.7}_{-4.7}$	$0.29^{+0.05}_{-0.04}$	$5.1^{+1.9}_{-2.8}$	296 / 247

*: Normalization of the apec component scaled with a factor $1/400\pi$.

Norm = $\frac{1}{400\pi} \int n_e n_H dV / (4\pi(1+z^2)D_A^2) \times 10^{-14} \text{ cm}^{-5} \text{ arcmin}^{-2}$, where D_A is the angular diameter distance to the source.

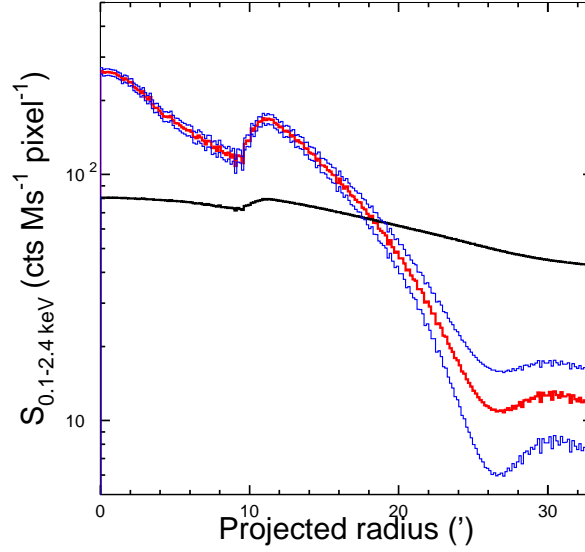


Fig. 6. Radial profile of the surface brightness. Red line show the ICM signal from A3376. Black line shows the background component. Two blue lines show the systematic errors considering fluctuations of the background component ($\pm 10\%$).

Voit, G. M., Balogh, M. L., Bower, R. G., Lacey, C. G., & Bryan,
G. L. 2003, *apj*, 593, 272
Wik, D. R., Sarazin, C. L., Finoguenov, A., et al. 2009, *ApJ*, 696, 1700